GEOPHYSICS, VOL. 71, NO. 4 (JULY-AUGUST 2006); P. G169–G177, 10 FIGS.
10.1190/1.2210847

Comparison of integral equation and physical scale modeling of the electromagnetic responses of models with large conductivity contrasts

Colin G. Farquharson[1], Ken Duckworth[2], and Douglas W. Oldenburg[3]

ABSTRACT

A comparison is made between the results from two different approaches to modeling geophysical electromagnetic responses: a numerical approach based upon the electric-field integral equation and the physical scale modeling approach. The particular implementation of the integral-equation solution was developed recently, and the comparison presented here is essentially a test of this new formulation. The implementation approximates the region of anomalous conductivity by a mesh of uniform cuboidal cells and approximates the total electric field within a cell by a linear combination of bilinear edge-element basis functions. These basis functions give a representation of the electric field that is divergence free but not curl free within a cell, and whose tangential component is continuous between cells. The charge density (which arises from the discontinuity of the normal com-

ponent of the electric field across interfaces between cells of different conductivities and between cells and the background) is incorporated in a similar manner to integral equation solutions to dc resistivity modeling. The scenarios considered for the comparison comprise a graphite cube of 6.3×10^4 S/m conductivity and 14-cm length in free space and in brine (7.3 S/m conductivity). The transmitter and receiver were small horizontal loops; measurements and computations were made for various fixed transmitter-receiver separations and various heights of the transmitter-receiver pair for frequencies ranging from 1–400 kHz. The agreement between the numerical results from the integral-equation implementation and the measurements from the physical scale modeling was very good, contributing to the verification of this particular implementation of the integral-equation solution to electromagnetic modeling.

INTRODUCTION

Quantitative interpretation of geophysical observations depends on the ability to model survey measurements, i.e., to synthesize the data that would have been acquired if the subsurface of the earth matched our particular representation of it. Altering the representation, or model, of the earth to make the synthesized data resemble the observed data as closely as possible presumably results in a model that resembles the actual subsurface of the earth. Of course, it is imperative that the technique used for the modeling process produces correct results, and that synthesized data generated by different modeling processes for the same survey and the same representation of the subsurface are equal. In this paper, we compare results from two completely different techniques for modeling the electromagnetic (EM) response of simple representations of the spatial variation of electrical conductivity in the earth. The two techniques are the numerical scheme of Farquharson and Oldenburg (2002), based

on a novel integral-equation formulation, and physical scale modeling in the vein of Duckworth and Krebes (1997) and Duckworth et al. (2001). Because of the independence of the two techniques, agreement between their respective synthesized data will strongly verify the correctness of both.

The models of electrical conductivity variation considered here specifically contain large contrasts. These are not obscure, irrelevant examples but in fact correspond to the classic and still important target for EM methods in geophysics: a highly conducting metallic orebody residing in resistive shield rocks (see, for example, Frischknecht et al., 1987; Palacky and West, 1987). Most existing integral-equation numerical modeling techniques fail for high contrasts. The desire to correct this failing motivated the development of the integral-equation formulation presented in Farquharson and Oldenburg (2002). And the desire to verify this formulation motivated the com-

parison with the results from physical scale modeling presented here.

The earliest numerical modeling techniques for geophysical EM survey data were for models comprising a simple, geometric object such as a sphere in a nonconducting whole space for which a boundary-value problem could be formulated and a series solution found (Wait, 1951, 1953; March, 1953). This style of technique developed because it could be implemented at the time and because the model was a fair approximation of the predominant exploration target of a localized, conductive orebody in a very resistive host. The evolution of numerical modeling proceeded with the pioneering of the volume integral approach by Raiche (1974), Hohmann (1975), and Weidelt (1975). Again, this technique was suited to a localized region of anomalous, distinct conductivity in an otherwise simple background model (an orebody in shield rocks) and was practical, given contemporaneous computing capabilities. As the speed and memory of computers increased, numerical modeling came to be dominated by finite-difference and finite-element formulations. These are better suited to general, complex models with variable, extensive features and are therefore more appropriate for constructing inversion programs. As a consequence, interest in integral-equation formulations waned and their development stalled.

However, there remained the unresolved issue of traditional integral-equation formulations failing for models containing large conductivity contrasts. Lajoie and West (1976), while developing their integral-equation solution for a finite, thin, conductive plate buried in a conductive background, noted that solving in the obvious manner for the components of the secondary electric field in the plate led to incorrect secondary fields for "any reasonably resistive" background. They attributed this to two factors: (1) the mixing of the effects of inductive, divergence-free current flow and conductive, curl-free current flow that happens when the background is not perfectly resistive and (2) the nontrivial issue of ensuring neither of these physical effects is unintentionally discarded when deriving the numerical formulation of the problem. Newman et al. (1986) have recognized that their volume integral-equation formulation works best for moderate contrasts, giving a ratio of 300:1 as typical of the contrast beyond which their solution breaks down. They attribute this failing to the domination of the galvanic conduction-current contribution over the induction-current contribution in their numerical formulation, even for models for which this was inappropriate. To overcome the problem for the thin plate, Lajoie & West solve for two scalar potentials corresponding to the divergence-free and curl-free components of the scattering current variation within the plate. For the volume integral equation, SanFilipo and Hohmann (1985) and Newman and Hohmann (1988) augment the set of traditional pulse basis functions for the secondary electric field in the anomalous region with groupings of pulse basis functions that explicitly form divergence-free current loops, using the Galerkin method to derive their numerical formulation. Thus, the term that previously led to the ever-present dominance of the galvanic contribution could be eliminated.

The formulation of SanFilipo and Hohmann (1985) and Newman and Hohmann (1988) for the volume integral equation did produce correct results for models with large contrasts in conductivity between the anomalous region and the background. However, because the current-tube basis functions are hard wired, the current systems in the anomalous region that can be represented are somewhat limited and are restricted to rather symmetric patterns. Recently there have been a number of attempts to find a more general, and arguably

more elegant, numerical formulation of the volume integral-equation solution to geophysical EM forward modeling. Slob and van den Berg (1999) expand the electric field within the anomalous region in terms of local trilinear functions, directly impose continuity of the tangential component of the electric field between neighboring cells, and contrive continuity of the normal component of current density in a least-squares sense. However, they do not report success for conductivity contrasts greater than 100:1. Xiong et al. (1999) derive a formulation of the electric-field integral equation that contains both volume integrals involving the scattering current density within the cells of uniform conductivity comprising the anomalous region and surface integrals involving surface charge densities between cells of different conductivities. Kim and Song (2001) use the same volume-surface integral-equation formulation of the electric-field integral equation and express the scattering current as the sum of a divergence-free, vortex current potential and a curl-free, current channeling potential. Kim and Song report successful application to the thin-sheet approximation. Farquharson and Oldenburg (2002) use a similar formulation of the electric-field integral equation, comprising volume integrals of the electric field within the cells and surface integrals of the charge densities between cells. They expand the electric field in terms of local bilinear edge-element basis functions that result in a divergence-free but not curl-free approximation of the electric field within each cell, and they impose continuity of the tangential component of the electric field via edge-element basis functions. They present comparisons between the results computed using their formulation for a cube of 100 S/m in a half-space of 10^{-4} S/m with results calculated for a sphere in a nonconducting whole space. The comparison of results from this formulation with those from physical scale modeling is the focus of this paper.

Physical scale modeling began almost as soon as EM exploration itself, thus predating numerical modeling by a couple of decades (see, for example, Frischknecht, 1987). With appropriate scaling of spatial dimensions and electrical properties and scaling of the frequency of the inducing field, equivalence can be achieved between measurements made in a laboratory and those for a full-sized survey over a full-sized, idealized geological feature. The styles of model most suitable for physical scale modeling are a single localized conductor in free space and a localized conductor in a homogeneous half-space, which are exactly the styles of model required for testing a numerical scheme based on a volume integral-equation formulation. However, all of the physical scale modeling that has been done, certainly for the magnetic dipole transmitter-receiver arrangements that are of interest here, has apparently been only for thin sheets or elongated rectangular prisms (see Frischknecht, 1987, and references therein) rather than an unequivocally 3D object such as a cube. Physical scale modeling surveys were therefore performed to generate data for comparison with the integral-equation technique presented here.

The remainder of this paper is organized as follows. First, brief descriptions are given of the integral-equation formulation being tested and of the laboratory apparatus used for the physical scale modeling. Then the comparison between numerical and physical scale modeling results is illustrated for a graphite cube (6.3×10^4 S/m, 14-cm side length) in free space and the same cube in brine (7.3 S/m) for a selection of the frequencies and transmitter-receiver separations for which data were measured and computed.

INTEGRAL-EQUATION NUMERICAL MODELING

We used the numerical modeling procedure of Farquharson and Oldenburg (2002). (Only the most salient features of the method are summarized below; see the aforementioned reference for a more detailed description).

The integral equation upon which the numerical implementation is based is

$$\mathbf{E} = \mathbf{E}_b + i\omega\mu \int_V \underline{\mathbf{G}}^{(1)} \cdot \mathbf{E}\Delta\sigma dv' + \int_V \mathbf{G}^{(2)}\nabla' \cdot \mathbf{E}dv'. \quad (1)$$

We assume that the variation of electrical conductivity σ within the model can be separated into a simple background conductivity σ_b for which electric and magnetic fields for the source of interest are readily available and a localized, anomalous region $\Delta\sigma$ of volume V:

$$\sigma(\mathbf{r}) = \sigma_b + \Delta\sigma(\mathbf{r}), \quad (2)$$

where $\mathbf{r}$ is the position vector. (We further assume that the background conductivity is a homogeneous half-space.) The electric field $\mathbf{E}$ that exists in the model can then be thought of as the sum of the electric field $\mathbf{E}_b$ that would exist if the anomalous region were not present and a secondary or scattered electric field $\mathbf{E}_s$ that is the difference between $\mathbf{E}_b$ and the field that actually exists:

$$\mathbf{E}(\mathbf{r}) = \mathbf{E}_b(\mathbf{r}) + \mathbf{E}_s(\mathbf{r}). \quad (3)$$

The background electric field satisfies the following differential equation:

$$-\nabla^2\mathbf{E}_b + \nabla(\nabla \cdot \mathbf{E}_b) - i\omega\mu\sigma_b\mathbf{E}_b = i\omega\mu\mathbf{J}^I, \quad (4)$$

and the secondary electric field satisfies

$$\nabla^2\mathbf{E}_s - \nabla(\nabla \cdot \mathbf{E}_s|_{z=0}) + i\omega\mu\sigma_b\mathbf{E}_s$$
$$= -i\omega\mu\Delta\sigma\mathbf{E} + \nabla(\nabla \cdot \mathbf{E}_s|_V), \quad (5)$$

where ω is angular frequency, μ is magnetic permeability (assumed to be constant throughout the model), and $\mathbf{J}^I$ is the current density corresponding to the impressed source. Also, the quasi-static approximation is invoked, a time dependence of $e^{-i\omega t}$ is assumed, and $i = \sqrt{-1}$. Furthermore, the divergence of the secondary electric field is separated into the contribution from the surface of the homogeneous half-space ($\nabla \cdot \mathbf{E}_s|_{z=0}$) and the contribution from the region of anomalous conductivity ($\nabla \cdot \mathbf{E}_s|_V$). Given the above differential equations and using the vector Green's functions $\mathbf{g}^k(\mathbf{r};\mathbf{r}')$, $k = x,y,z$, which satisfy

$$\nabla^2\mathbf{g}^k - \nabla(\nabla \cdot \mathbf{g}^k) + i\omega\mu\sigma_b\mathbf{g}^k = -\delta(\mathbf{r} - \mathbf{r}')\hat{\mathbf{u}}_k, \quad (6)$$

where $\hat{\mathbf{u}}_k$ is the unit vector in the kth direction, equation 1 can be arrived at in the usual manner. The tensor and vector Green's functions in equation 1 are, in general terms,

$$\underline{\mathbf{G}}^{(1)} = \begin{bmatrix} g_x^x & g_y^x & g_z^x \\ g_x^y & g_y^y & g_z^y \\ g_x^z & g_y^z & g_z^z \end{bmatrix} \quad \text{and} \quad \mathbf{G}^{(2)} = \begin{bmatrix} \nabla' \cdot \mathbf{g}^x \\ \nabla' \cdot \mathbf{g}^y \\ \nabla' \cdot \mathbf{g}^z \end{bmatrix}. \quad (7)$$

Our integral equation method is significant in its numerical implementation, which is summarized below. However, the electric-field integral equation as written in equation 1 exhibits some appealing characteristics (which anticipate the particulars of the numerical implementation). At zero frequency, this arrangement of the integral equation reduces without further manipulation to the integral equation for the dc resistivity modeling problem presented by Snyder (1976). Also, the two integrals in equation 1 effectively divide the secondary electric field into an inductive, divergence-free part and a galvanic, curl-free part. The former is associated with the extra current density $\Delta\sigma\mathbf{E}$ flowing in, and because of, the region of anomalous conductivity. The latter is associated with the accumulation of charge $\nabla \cdot \mathbf{E}$ on the boundary of the region of anomalous conductivity and at places within this region where the conductivity is changing.

The region of anomalous conductivity is discretized into a regular mesh of cuboidal cells. The conductivities of the cells can vary from one to another, but it is assumed that the conductivity within a cell is uniform. The total electric field within the region of anomalous conductivity is approximated by a linear combination of basis functions:

$$\mathbf{E}(\mathbf{r}) \approx \sum_{j=1}^N c_j\mathbf{v}_j(\mathbf{r}). \quad (8)$$

There are twelve basis functions to a cell (which are zero everywhere outside the cell). Four are directed in the x-direction and vary bilinearly with y and z, four are y-directed and vary bilinearly with x and z, and four are z-directed and vary bilinearly with x and y. Because of this, the approximation of the electric field within a cell has zero divergence, which should be the case for an electric field in a region of uniform conductivity. In addition, these basis vectors are such that the approximate electric field within a cell can have a nonzero curl (although only constant). The basis functions are specified such that each of the four x-directed basis functions in a cell is equal to unity on one of the x-directed edges of its cell and zero on the three other x-directed edges, and likewise for the y- and z-directed basis functions. Furthermore, when two cells share a face, the basis functions in the two cells that share the common edges are tied together to form combined, composite basis functions that extend across the two cells. Hence, the tangential component of the approximate electric field is continuous across interfaces between neighboring cells, again something a genuine electric field exhibits. The basis functions described above are known as edge-element basis vectors.

Equation 1 can be thought of abstractly as the operator equation

$$\mathbf{L}[\mathbf{E}] = \mathbf{E}_b, \quad (9)$$

where the linear operator $\mathbf{L}$ involves the two integrals in equation 1 and the identity operator. (The two integral terms are considered later.) Substituting the approximation for the electric field given by equation 8 into equation 9 gives

$$\sum_{j=1}^N c_j\mathbf{L}[\mathbf{v}_j] = \mathbf{E}_b + \mathbf{R}, \quad (10)$$

where $\mathbf{R}$ is the residual because of the approximate nature of the representation of the electric field. The Galerkin variant of the method of weighted residuals (see, for example, Hohmann, 1987) is used to construct a system of equations. Specifically, the inner product of each basis function with equation 10 gives N simultaneous equations:

$$\underline{\mathbf{A}}\mathbf{x} = \mathbf{b}, \quad (11)$$

where $A_{ij} = \langle \mathbf{v}_i, \mathbf{L}[\mathbf{v}_j] \rangle$, $x_i = c_i$, $b_i = \langle \mathbf{v}_i, \mathbf{E}_b \rangle$, and $\langle \mathbf{u}, \mathbf{w} \rangle = \int_V \mathbf{u} \cdot \mathbf{v} dv$. It is assumed that requiring $\mathbf{R}$ to be orthogonal to the basis functions (that is, $\langle \mathbf{v}_j, \mathbf{R} \rangle = 0 \; \forall j$), as is done in forming equation 11, results in a good approximation for the electric field.

The component of the linear operator in equation 10 corresponding to the first integral in equation 1 is

$$\mathbf{L}^{(1)}[\mathbf{v}_j] = i\omega\mu \int_{V_J} \underline{\mathbf{G}}^{(1)} \cdot \mathbf{v}_j \Delta\sigma \, dv', \qquad (12)$$

where V_J is the volume of the cell in which $\mathbf{v}_j$ is not zero. Since the region of anomalous conductivity is discretized into uniform cells, the divergence of the electric field is nonzero only on the interfaces between cells of differing conductivities and between the cells on the edge of the anomalous region and the background. The divergence can then be expressed in terms of a surface charge density, which is related to the jump in the normal component of the electric field at the interface. This means the component of the linear operator in equation 10 arising from the second integral in equation 1 becomes

$$\mathbf{L}^{(2)}[\mathbf{v}_j] = \int_{\partial V_J} \mathbf{G}^{(2)} \left(\frac{\sigma_J}{\sigma_n} - 1 \right) \mathbf{v}_j \cdot \hat{\mathbf{n}} ds', \qquad (13)$$

where σ_n is the conductivity of the relevant neighboring cell or of the background. This surface integration is the same as what is done in integral-equation solutions to the dc resistivity modeling problem (Snyder, 1976). It is also this term and its explicit dependence on the conductivity in neighboring cells (and that of the background for cells on the edge of the anomalous region) which are responsible for keeping currents in the numerical solution contained within regions of high conductivity when they are isolated within regions (or a background) of low conductivity.

Hence, once the discretization of the region of anomalous conductivity for a particular problem has been decided upon, the system of equations given by equation 11 is formed by performing the various inner product integrations. All integrations, both volume and surface, are done using Gaussian quadrature. For simplicity, the Green's functions are approximated at this stage by their whole-space incarnations, meaning $\mathbf{G}^{(1)}$ is a diagonal tensor with elements equal to the familiar, scalar whole-space Green's function:

$$g_x^x = g_y^y = g_z^z = g^w(\mathbf{r};\mathbf{r}') = \frac{1}{4\pi} \frac{e^{ik_b|\mathbf{r}-\mathbf{r}'|}}{|\mathbf{r} - \mathbf{r}'|}, \qquad (14)$$

where $k_b^2 = i\omega\mu\sigma_b$, and

$$\mathbf{G}^{(2)} = \begin{bmatrix} \partial g^w / \partial x' \\ \partial g^w / \partial y' \\ \partial g^w / \partial z' \end{bmatrix} = \nabla' g^w. \qquad (15)$$

The singularities of the integrals in equations 12 and 13 can be ignored because they do not contribute to the inner product integrations of the Galerkin approach (see Farquharson and Oldenburg, 2002). Once equation 11 has been solved and hence the approximation of the total electric field within the region of anomalous conductivity obtained, the integral equation (equation 1) is used to compute the electric (or magnetic) field wherever it is required. These calculations also involve equations 12 and 13 but with the half-space forms of the Green's functions.

PHYSICAL SCALE MODELING

The apparatus used to acquire the physical scale modeling results presented in this paper is the same as that used by Duckworth and Krebes (1997) and Duckworth et al. (2001) in their studies of the consequences of current gathering when a target is located within conductive host rocks. It is similar to that of Gupta Sarma and Maru (1971) and Gaur et al. (1972), who also investigate the effects of a conducting host. (For a comprehensive review of physical scale modeling, including technical aspects of sources, receivers, and materials as well as a review of the literature, see Frischknecht, 1987.)

Figure 1 shows a photograph of the physical scale modeling apparatus. The tank for holding the brine is 5 m long, 3 m wide, and 1.3 m deep. The conductivity of the brine for the sequence of measurements for which it was present is 7.3 S/m. The 3D target for all examples presented in this paper was a graphite cube with a side length of 14 cm and a conductivity of 6.3×10^4 S/m. The transmitter and receiver are small horizontal loops of wire, and data are acquired along profiles over the graphite cube for various different fixed separations between the transmitter and receiver and for different heights of the transmitter-receiver pair above the cube. The collection of each profile is automated, with measurements made every 5 mm (with a repeatability of ± 0.5 mm). The data generated by the apparatus and subsequent processing are the in-phase and quadrature parts of the secondary magnetic field, that is, the total field minus the free-space field for the particular transmitter-receiver separation, normalized by the free-space field. Data were collected for frequencies of the sinusoidal current in the transmitter loop ranging from 1–400 kHz.

In the following section, the numerical and physical scale modeling results are compared directly for the dimensions, conductivities, and frequencies of the physical-scale model. However, any scenario for which the induction number $\sigma f l^2$ is the same as that of the physical model, where σ is conductivity, f is frequency, and l is a characteristic length (and the magnetic permeability is the same everywhere in the model and the full-scale system, and the quasi-static assumption is valid), will generate the same response. For example, the secondary magnetic fields shown here for the cube of 14 cm and 6.3×10^4 S/m for frequencies of 1–400 kHz would be equivalent to those observed over a cube of 140 m and 6.3×10^{-1} S/m for frequencies 100 Hz to 40 kHz (with the brine conductivity of 7.3 S/m scaling to a host-rock conductivity of 7.3×10^{-5} S/m).

Figure 1. The apparatus used to acquire the physical scale modeling data presented in this paper.

EXAMPLES

Four examples are presented here. The first two are for a 20-cm separation between the transmitter and receiver, with the transmitter-receiver pair passing 4 cm over a cube in free space and then in brine. Example 3 is for the transmitter-receiver pair at successively greater heights above the cube (in free space). The fourth example is for a transmitter-receiver pair at its maximum possible height with the cube immersed in brine.

Example 1

The first example is for the graphite cube in free space and for a transmitter-receiver pair of 20-cm separation passing over the cube at a height of 4 cm. Measurements were made and numerical forward modeling was done for 1, 2, 4, 10, 20, 40, 100, 200, and 400 kHz. The results for 1, 10, 100, 200, and 400 kHz are shown in Figure 2.

For the integral-equation modeling for this and all following examples, the cube was discretized into $10 \times 10 \times 10$ cells of equal size, with $2 \times 2 \times 2$ nodes used for the Gaussian quadrature for the volume integrals and with 5×5 nodes for the Gaussian quadrature for the surface integrals. A free-space background could not be modeled per se using the implementation of the integral-equation method presented here. Instead, the cube was considered to be within a homogeneous half-space of 10^{-4} S/m (which extended up to the height of the transmitter-receiver pair). Also, the implementation is computationally intensive; the time required for the number of cells and nodes mentioned above was roughly eight days on a 1-GHz Pentium III computer, virtually all of which was spent calculating the elements of the matrix. The discretization of $10 \times 10 \times 10$ cells was therefore the largest number of cells considered.

Responses obtained with moving-source, dipole-type EM systems such as those being investigated here are known to display reciprocity. At any given location of the transmitter-receiver pair, an interchange of the transmitter and receiver will produce an identical response. This concept requires that any response profile obtained over a symmetrical conductor will also be symmetrical; yet interchanging the transmitter and receiver at a location where one coil is over the center of the target conductor and the other is off the flank of the conductor must result in a very different pattern and magnitude of induced currents within the conductor. Given this disparity of the induced currents, the reciprocity of response that results is perhaps remarkable.

The geometry of this example (see Figure 2) provided strong secondary fields because of the small ratio of conductor depth to coil separation (0.2). The consequently large S/N ratio in the physical modeling permitted high-quality data to be obtained easily. The physical model responses shown in Figure 2 display the expected symmetry, which indicates reciprocity. By comparison, the discretization used in the numerical modeling was not sufficiently fine for

the rapid spatial variation of the electric field within the cube for this small depth-to-separation ratio and for the transmitter directly above the cube to be simulated accurately. The asymmetrical deviations of the numerical profiles in Figure 2 as the transmitter passes over the cube (that is, for locations of the center of the transmitter-receiver pair between approximately 25 and 40 cm) are a result of the inadequacies of the discretization. Figure 3 shows two profiles for 10 kHz produced by the numerical modeling — one with the transmitter to the left of the receiver (the same as for Figure 2) and the other with the transmitter to the right of the receiver. Although neither curve is symmetric, they are mirror images of each other about the center of the cube, with their respective asymmetrical deviations correspond-
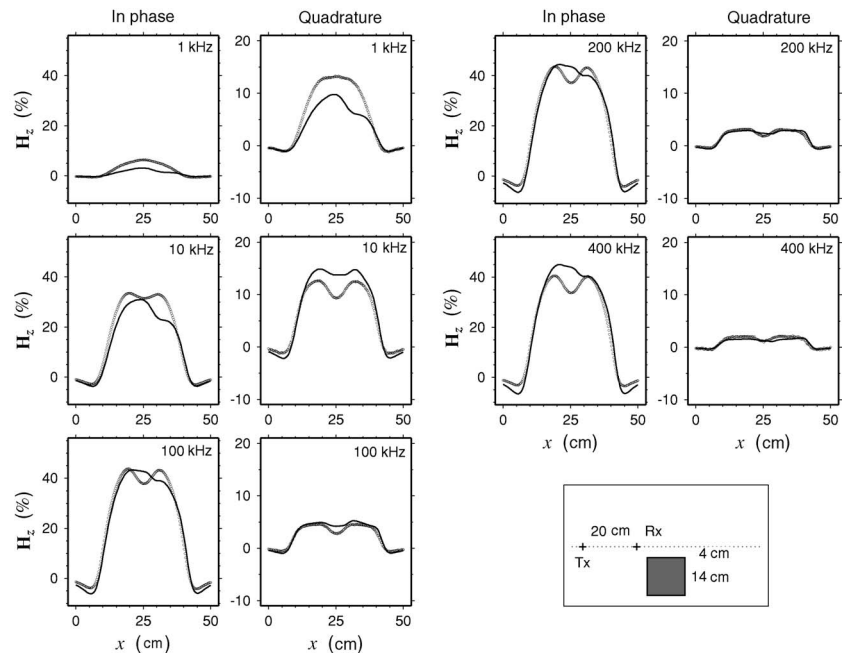

Figure 2. The results for the cube in free space, with the transmitter-receiver pair having a separation of 20 cm and passing at a height of 4 cm over the cube. The circles are for the physical scale modeling results, and the solid lines are for the integral equation results. The abscissa is the location of the center of the transmitter-receiver pair. (The center of the cube is directly below $x = 25$ cm.) The ordinate is the secondary H-field (i.e., total minus free space) normalized by the free-space H-field for this separation and orientation of the transmitter and receiver. (The diagram of the arrangement of the cube and of the transmitter and receiver is to scale).
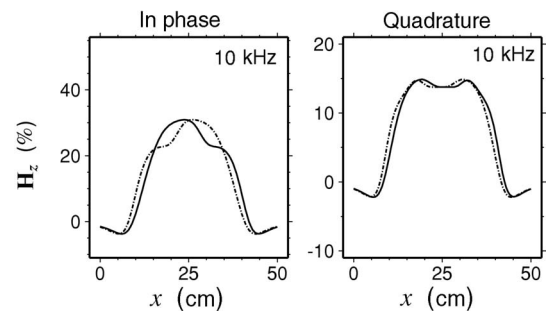

Figure 3. The numerical modeling results for 10 kHz for the first example when the transmitter is to the left of the receiver (solid line; see Figure 2) and when the transmitter is to the right of the receiver (broken line). The abscissa is the location of the center of the transmitter-receiver pair.
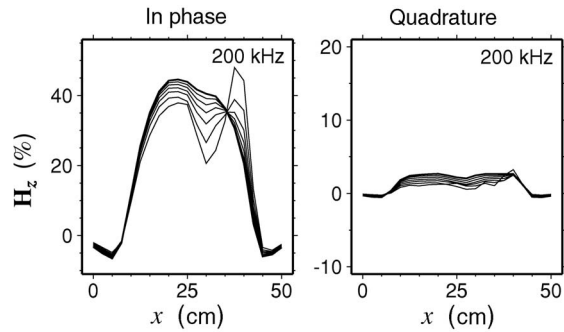
Figure 4. The numerical modeling results for 200 kHz for the first example (see Figure 2) for discretizations of 4 × 4 × 4 to 10 × 10 × 10 cells. The heavier line indicates the 10 × 10 × 10 discretization.
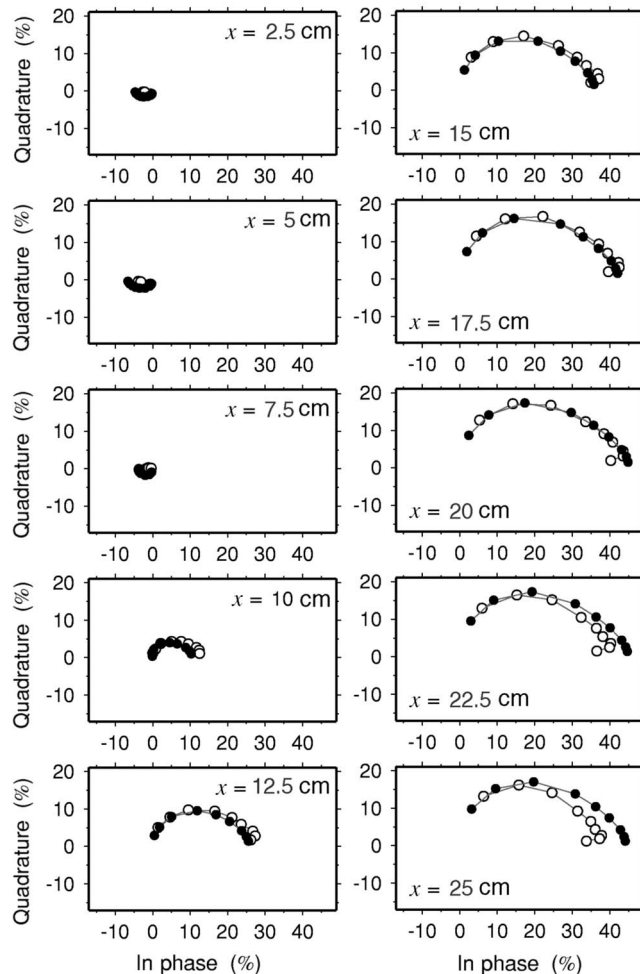

Figure 5. Argand diagrams of the physical scale modeling results (open circles) and the integral-equation results (filled circles) for the cube in free space and the transmitter-receiver pair 4 cm above the cube with a separation of 20 cm. The panels are for ten different locations of the transmitter-receiver pair spaced at 2.5-cm intervals from x = 2.5 to 25 cm. Results are plotted for nine frequencies: 1, 2, 4, 10, 20, 40, 100, 200, and 400 kHz. The points move away from the origin in this sequence of increasing frequency.

ing to when the transmitter is over the cube. Also, Figure 4 shows how the numerical modeling results for 200 kHz improve with successively finer discretizations (from 4 × 4 × 4 to 10 × 10 × 10 cells). Irrespective of the deficiencies of the discretization used for this example, the agreement, illustrated by Figure 2, between the physical scale modeling measurements and the values computed by the integral equation method is good, especially considering the conductivities and geometry involved.

The noteworthy features of the responses illustrated in Figure 2 are as follows. The amplitude of the in-phase anomalies increases with frequency, and the rate of increase diminishes at the highest frequencies considered here. The amplitude of the quadrature anomalies initially increases with frequency (although this is not discernible from the selection of frequencies plotted in Figure 2) before decreasing, as expected for a response approaching the inductive limit. The quadrature anomaly displays greater amplitude than the in-phase anomaly at the lowest frequencies, but at moderate and higher frequencies the in-phase anomaly amplitude surpasses the quadrature amplitude. A small loss of anomaly amplitude is evident in both the in-phase and quadrature curves for all but the lowest frequencies when the center of the transmitter-receiver pair is directly over the center of the cube. Small symmetrical negative excursions are present in both the in-phase and quadrature curves for all frequencies as the cube is approached.

Figure 5 shows the responses for this example displayed in the form of Argand diagrams. The abscissa and ordinate are the in-phase and quadrature parts, respectively, of the normalized secondary H-field. The responses for all nine frequencies (1, 2, 4, 10, 20, 40, 100, 200, and 400 kHz) are shown. The ten panels in this figure are for ten different locations of the transmitter-receiver pair spaced at 2.5-cm intervals from x = 2.5 to 25 cm. (This last location corresponds to the center of the transmitter-receiver pair being directly over the center of the cube.) All of the curves trend as clockwise, quasi-semicircular arcs outward from the origin as the frequency increases. The curves for the three locations farthest from the cube (x = 2.5, 5, and 7.5 cm) correspond to the negative excursion caused by the edge effect in the response as shown in Figure 2 for which both the in-phase and quadrature values are negative. The uncomplicated nature of the curves in the Argand diagrams is characteristic of the single mechanism of induction within the cube which is giving rise to the responses.

Example 2

Next, results are presented for the same disposition of cube and transmitter-receiver pair used in the preceding example but with the cube immersed in brine. The surface of the brine was 2 cm above the top of the cube, and the transmitter-receiver pair was 2 cm above the surface of the brine. (As mentioned previously, the conductivity of the brine was 7.3 S/m.) The same range of frequencies as Example 1 was investigated. The results for 1, 10, 100, 200, and 400 kHz are shown in Figure 6. (The secondary field as plotted in Figure 6 is the total field minus the free-space field, normalized by the free-space field.)

The responses for this example are similar to those for Example 1 (see Figure 2), which is not surprising, considering that the contrast in conductivity between the cube and the brine is still large. The only clear difference in how the in-phase curves change with frequency is that the half-space response, which is apparent at the ends of the profiles, becomes appreciable and negative at the highest frequencies.

The discrepancy between the scale modeling and numerical results for the in-phase values at 400 kHz that can be seen in Figure 6 is thought to be from a capacitive effect in the physical scale modeling apparatus (which was not treated by the numerical modeling). At high frequencies, the physical scale modeling coils displayed capacitive responses to nonconductive polar materials such as Plexiglas and water. At the highest frequencies investigated here, this capacitive interaction between the coils and the ion-saturated water (the conductive host) appears to have counteracted the inductive interaction with the water.

The half-space quadrature response for this example also becomes negative as the frequency increases but more gradually than the in-phase response. At the two highest frequencies, the quadrature response over the cube is different from that for Example 1 from which the brine is absent. The anomaly amplitude remains small over the cube despite the half-space quadrature response becoming more negative. The loss of anomaly amplitude when the center of the transmitter-receiver pair is over the center of the cube, evident at intermediate frequencies (and at the higher frequencies in Example 1), becomes a small positive increase in anomaly amplitude that can be seen in both the numerical and physical scale modeling results.

The Argand diagrams of the responses for this example are shown in Figure 7. The abscissa and ordinate in this figure are the in-phase and quadrature parts, respectively, of the total H-field minus the half-space H-field, normalized by the free-space field. This figure therefore isolates the component of the response that results from the presence of the conducting cube. (The in-phase and quadrature parts of the total H-field minus the free-space field, normalized by the free-space field, for the brine alone are shown in the inset in the top

left panel of Figure 7.) The responses for the first four locations of the transmitter-receiver pair illustrated in Figure 7 ($x = 2.5$, 5, 7.5, 10 cm) are similar to the corresponding responses without the brine (see Figure 5); the responses are small, but they exhibit an arclike trend outward from the origin with increasing frequency. However, as the transmitter-receiver pair move closer to a location over the cube, a small upward tail to the arclike trend appears for the highest few frequencies, both in the physical-scale and numerical modeling results. Similar tails, and some considerably larger, have been observed for other situations involving a conductor in a conductive host, most notably in the responses over a vertical conducting plate offset from a large, fixed transmitter loop (Duckworth et al., 2001). This and the other situations in which these tails have previously been observed have an arrangement of transmitter and conductor that is good for gathering or channeling current from the conductive host into the conductor. The tails in the Argand diagrams, which indicate an enhancement of the response, are attributed to the onset of these current-gathering effects. The existence of the distinctive tails in Figure 7, even though they are relatively small, is evidence of such effects contributing to the responses for the situation considered here (that is, moving transmitter-receiver pair, localized conductor), one in which a noticeable contribution from these effects might not have been anticipated.

Finally, for this example, Figure 8 shows the response profiles for 200 kHz computed using the classic implementation of the integral equation solution, that of Hohmann (1987). This implementation approximates the electric field using pulse basis functions, uses delta weighting functions in the method of weighted residuals, and approximates the surface and volume integrations for the cuboidal cells by analytic expressions for integrations over spheres of equivalent volumes. It is clear from Figure 8 that this implementation fails to reproduce the response, especially its strength, for this situation in which the conductivity contrast is four orders of magnitude. Figure 8 also shows the responses computed using the implementation presented in this paper with the explicit dependence on the conductivities in neighboring cells in the integration of surface charge density (see equation 13) replaced by background conductivity. This is as if all of the cuboidal cells discretizing the anomalous region had been separated ever so slightly from one another, with slivers of the background material filling the gaps. The responses computed using this modification resemble those computed using the traditional approach, especially in the way in which they both fail to match the strength of the actual responses. Therefore, the inclusion of the explicit dependence on the conductivities of neighboring cells, and hence continuity of the normal component of current density, appears to be the aspect of the implementation of our integral-equation formulation that makes it successful for large conductivity contrasts.
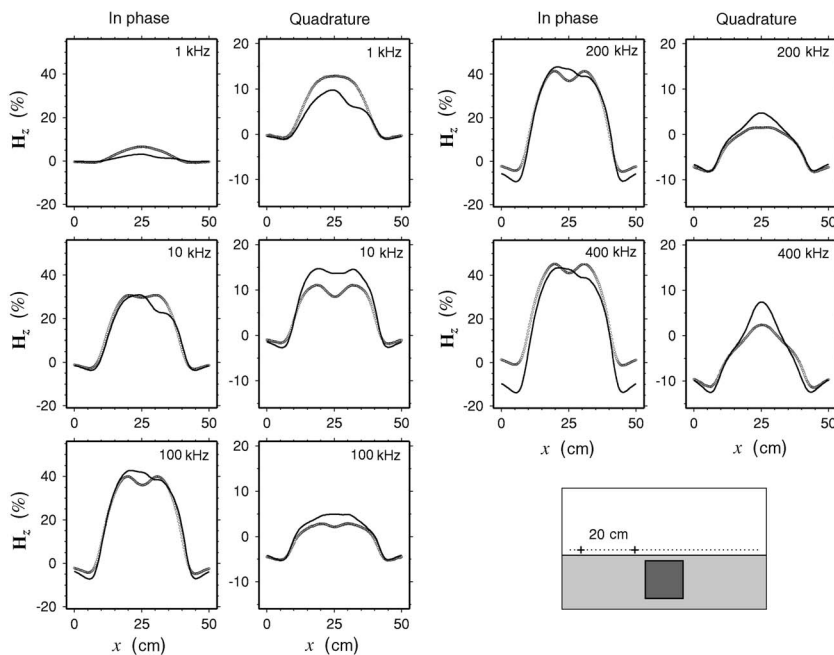

Figure 6. The results for the cube in brine. The surface of the brine was 2 cm above the top of the cube, and the transmitter-receiver pair was 2 cm above the surface of the brine. (The conductivity of the graphite cube was 6.3×10^4 S/m; that of the brine was 7.3 S/m.) As for the first example, the separation between transmitter and receiver was 20 cm. The circles represent the scale-modeling measurements; the lines are the numerical modeling values. The ordinate is the secondary H-field (i.e., total minus free space) normalized by the free-space H-field for this separation and orientation of the transmitter and receiver.

Example 3

The third example is for increasing heights (4, 6, and 8 cm) of the transmitter-receiver pair

above the cube in free space. The results for a frequency of 100 kHz and a transmitter-receiver separation of 10 cm are shown in Figure 9.

As the transmitter moves higher above the cube, and hence the spatial variation of the primary magnetic field that the cube experiences lessens, the discretization of the numerical modeling proce-
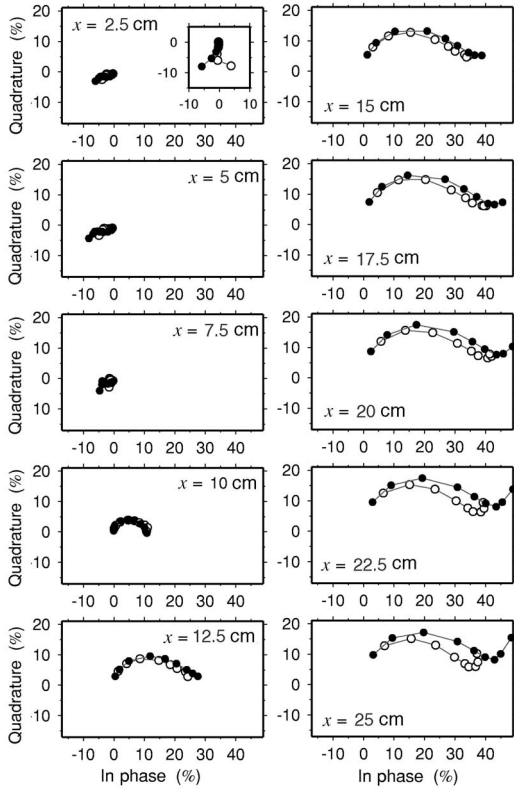

Figure 7. Argand diagrams for the cube in brine, with the top of the cube 2 cm below the surface of the brine and the transmitter-receiver pair 2 cm above the brine. (The transmitter-receiver separation was 20 cm.) The open circles are for the physical scale modeling measurements; the filled circles are the integral equation values. Results are plotted for 1, 2, 4, 10, 20, 40, 100, 200, and 400 kHz, with the movement of the plotted points outward from the origin following this sequence of frequencies. The abscissa and ordinate are the in-phase and quadrature parts, respectively, of the normalized total H-field minus the half-space field. (The inset in the top left panel shows the curves for the brine without the cube, total minus free-space field).
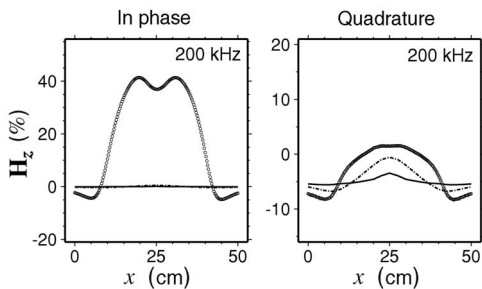

Figure 8. The responses for the cube in brine for 200 kHz computed using pulse basis functions and equivalent spheres (solid lines) and using bilinear basis functions with no continuity of normal current density between neighboring cells (broken lines). The circles are the physical scale-modeling results (see Figure 6).

dure can better reproduce the electric field within the cube. By a profile height of 8 cm, the computed responses are almost completely symmetrical and match the measured responses very well. Even at the profile height of 4 cm, there is very good correspondence between the features in the physical scale modeling results and those in the numerical results.

Example 4

This final example is for the transmitter-receiver pair at a height of 13 cm above the surface of the brine, with the top of the cube 1 cm below the surface of the brine. The transmitter-receiver separation was 10 cm. The results for 200 kHz are shown in Figure 10.

The distance of the transmitter-receiver pair from the brine and the cube was the largest that could be managed by the physical scale modeling apparatus with an acceptable S/N ratio. As can be seen from Figure 10, there is excellent agreement between the physical scale modeling measurements and the numerical modeling results — even for the quadrature values, which show a poor S/N ratio at this height and the consequently large depth-to-separation ratio of 1.3. Tests of the physical modeling system and computer simulations
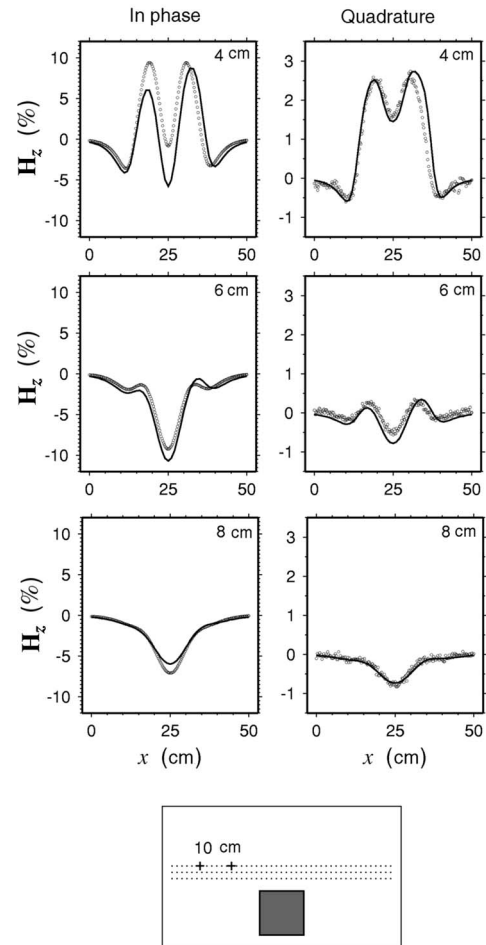

Figure 9. The results for the transmitter–receiver pair at heights of 4, 6, and 8 cm above the top of the cube with no brine present. The results shown are for a frequency of 100 kHz, and a transmitter-receiver separation of 10 cm. The circles and lines indicate the results of the scale and numerical modeling, respectively.
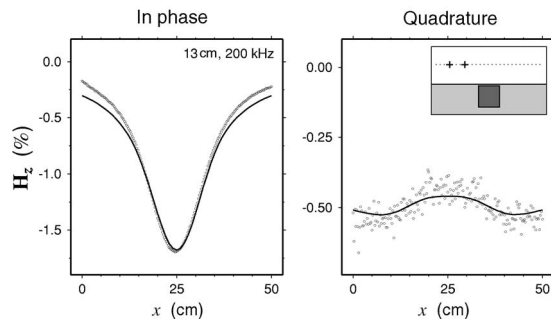
Figure 10. Results for the cube in brine with the top of the cube 1 cm below the surface of the brine, the transmitter-receiver pair at a height of 13 cm above the surface of the brine, and a transmitter-receiver separation of 10 cm. The frequency was 200 kHz. The circles show the physical scale-modeling results, and the lines show the numerical modeling results.

of the noise in that system indicate the noise in the quadrature component was caused by a phase jitter associated with the digital triggering of the oscilloscope and a secondary effect from amplitude-modulated random noise modulated by the signal itself. This meant the noise was at a maximum in the quadrature component of the signal. The mismatch between the in-phase values at the ends of the profile is because of the capacitive effects in the physical scale modeling apparatus, just as for Example 2.

CONCLUSIONS

A comparison of numerical modeling results and physical scale modeling measurements for a conducting cube in free space and in a conducting host has been presented. The numerical results were computed using a new implementation of the electric-field volume integral equation, one in which the electric field is approximated using bilinear edge-element basis functions and in which the normal component of the electric field between cells is related explicitly to the contrast in conductivity. The scale-model measurements were made using an apparatus designed to investigate the behavior of EM exploration systems over conductive features residing in a conductive host. The agreement between the numerical and scale-modeling results is good, helping to verify the implementation of the integral-equation solution, even for the challenging scenarios considered in this paper.

ACKNOWLEDGMENTS

REFERENCES

Duckworth, K., and E. S. Krebes, 1997, The response of steeply dipping tabular conductors located in conductive host rocks when detected by horizontal coplanar coil and vertical coincident coil electromagnetic exploration systems: Canadian Journal of Exploration Geophysics, **33**, 55–65.

Duckworth, K., T. D. Nichols, and E. S. Krebes, 2001, Examination of the relative influence of current gathering on fixed loop and moving source electromagnetic surveys: Geophysics, **66**, 1059–1066.

Farquharson, C. G., and D. W. Oldenburg, 2002, An integral equation solution to the geophysical electromagnetic forward-modelling problem, *in* M. S. Zhdanov and P. E. Wannamaker, eds., Three-dimensional electromagnetics: Elsevier, Inc., 3–19.

Frischknecht, F. C., 1987, Electromagnetic physical scale modeling, *in* M. N. Nabighian, ed., Electromagnetic methods in applied geophysics, vol. 1: SEG, 365–441.

Frischknecht, F. C., V. F. Labson, B. R. Spies, and W. L. Anderson, 1987, Profiling methods using small sources, *in* M. N. Nabighian, ed., Electromagnetic methods in applied geophysics, vol. 2: SEG, 105–270.

Gaur, V. K., O. P. Verma, and C. P. Gupta, 1972, Enhancement of electromagnetic anomalies by a conducting overburden: Geophysical Prospecting, **20**, 580–604.

Gupta Sarma, D., and V. M. Maru, 1971, A study of some effects of a conducting host rock with a new modeling apparatus: Geophysics, **36**, 166–183.

Hohmann, G. W., 1975, Three-dimensional induced polarization and electromagnetic modeling: Geophysics, **40**, 309–324.

——, 1987, Numerical modeling for electromagnetic methods of geophysics, *in* M. N. Nabighian, ed., Electromagnetic methods in applied geophysics, vol. 1: SEG, 313–363.

Kim, H. J., and Y. Song, 2001, A no-charge integral equation formulation for three-dimensional electromagnetic modeling: Butsuri-Tansa, **54**, 103–107.

Lajoie, J. J., and G. F. West, 1976, The electromagnetic response of a conductive inhomogeneity in a layered earth: Geophysics, **41**, 1133–1156.

March, H. W., 1953, The field of a magnetic dipole in the presence of a conducting sphere: Geophysics, **18**, 671–684.

Newman, G. A., and G. W. Hohmann, 1988, Transient electromagnetic responses of high-contrast prisms in a layered earth: Geophysics, **53**, 691–706.

Newman, G. A., G. W. Hohmann, and W. L. Anderson, 1986, Transient electromagnetic response of a three-dimensional body in a layered earth: Geophysics, **51**, 1608–1627.

Palacky, G. J., and G. F. West, 1987, Airborne electromagnetic methods, *in* M. N. Nabighian, ed., Electromagnetic methods in applied geophysics, vol. 2: SEG, 811–879.

Raiche, A. P., 1974, An integral equation approach to 3D modeling: Geophysical Journal of the Royal Astronomical Society, **36**, 363–376.

SanFilipo, W. A., and G. W. Hohmann, 1985, Integral equation solution for the transient electromagnetic response of a three-dimensional body in a conductive half-space: Geophysics, **50**, 798–809.

Slob, E. C., and P. M. van den Berg, 1999, Integral-equation method for modeling transient diffusive electromagnetic scattering, *in* M. L. Oristaglio and B. R. Spies, eds., Three-dimensional electromagnetics: SEG, 42–58.

Snyder, D. D., 1976, A method for modeling the resistivity and IP response of two-dimensional bodies: Geophysics, **41**, 997–1015.

Wait, J. R., 1951, A conducting sphere in a time varying magnetic field: Geophysics, **16**, 666–672.

——, 1953, A conducting permeable sphere in the presence of a coil carrying an oscillating current: Canadian Journal of Physics, **31**, 670–678.

Weidelt, P., 1975, Electromagnetic induction in three-dimensional structures: Journal of Geophysics, **41**, 85–109.

Xiong, Z., A. Raiche, and F. Sugeng, 1999, A volume-surface integral equation for electromagnetic modeling, *in* M. L. Oristaglio and B. R. Spies, eds., Three-dimensional electromagnetics: SEG, 90–100.